Structural joint inversion of time-lapse crosshole ERT and GPR traveltime data

[1]Joseph Doetsch, [2]Niklas Linde, [3]Andrew Binley

[1]Institute of Geophysics, ETH Zurich, Zurich, Switzerland; [2]Institute of Geophysics, University of Lausanne, Lausanne, Switzerland; [3]Lancaster Environment Centre, Lancaster University, Lancaster, U.K.

Abstract

Time-lapse geophysical monitoring and inversion are valuable tools in hydrogeology for monitoring changes in the subsurface due to natural and forced (tracer) dynamics. However, the resulting models may suffer from insufficient resolution, which leads to underestimated variability and poor mass recovery. Structural joint inversion using cross-gradient constraints can provide higher-resolution models compared with individual inversions and we present the first application to time-lapse data. The results from a synthetic and field vadose zone water tracer injection experiment show that joint 3-D time-lapse inversion of crosshole electrical resistance tomography (ERT) and ground penetrating radar (GPR) traveltime data significantly improve the imaged characteristics of the point injected plume, such as lateral spreading and center of mass, as well as the overall consistency between models. The joint inversion method appears to work well for cases when one hydrological state variable (in this case moisture content) controls the time-lapse response of both geophysical methods.

1. Introduction

Time-lapse geophysical monitoring and inversion are valuable tools in a wide range of application areas, such as hydrogeology, seismology, volcanology, landslide studies, and reservoir management. By inverting for temporal changes in geophysical properties it is possible to focus on resolving changes in state variables, such as water content and pore water salinity. The quality and resolution of time-lapse inversion results may also improve compared with static inversions as modeling and observational errors are generally smaller [e.g., *LaBrecque and Yang*, 2001]. Time-lapse inversion results are, unfortunately, also resolution-limited, leading to models that might be physically implausible or the resolved scales might be larger than those of interest [e.g., *Day-Lewis et al*., 2005]. Well known problems include the difficulty of recovering the injected mass of tracer or water from time-lapse inversion results [e.g. *Binley et al*., 2002a] and significant smearing in the horizontal directions [*Singha and Gorelick*, 2005] that reduce the value of geophysical time-lapse models in quantitative flow and transport studies.

Structural joint inversions of geophysical data acquired under static field conditions provide geometrically similar models and improve model resolution compared with individual inversions [e.g., *Gallardo and Meju*, 2004; *Linde et al*., 2008]. We focus here, for the first time, on the applicability of a structural joint inversion approach to time-lapse data. Structure is imposed by penalizing deviations from cases when the gradients - for different geophysical properties - of the total model updates from background models point in the same or opposite directions. These background models are obtained by inversion of the data acquired prior to any perturbation. We investigate the merits of this cross-gradient-constrained joint inversion using a synthetic and field vadose zone water-injection experiment, both of which employ time-lapse crosshole electrical resistivity tomography (ERT) data and first-arrival ground-penetrating radar

(GPR) traveltimes. Under these conditions, the time-lapse changes in both data types are related solely to variations in moisture content.

2. Methods

2.1. Time-lapse inversion strategy

The first step of our time-lapse inversion strategy is to obtain background (and initial) models of the logarithm of electrical resistivity ($\mathbf{m}_{\mathbf{e},0}$) and radar slowness ($\mathbf{m}_{\mathbf{r},0}$) by inverting data sets acquired prior to any perturbations. The data are inverted following an Occam's type inversion by penalizing differences from a homogeneous model as defined by an exponential covariance model [*Linde et al*., 2006]. We then use a difference inversion approach to invert the time-lapse data [e.g., *LaBrecque and Yang*, 2001] in which we, in a similar manner, penalize deviations from $\mathbf{m}_{\mathbf{e},0}$ and $\mathbf{m}_{\mathbf{r},0}$.

For the ERT inversions, we use an error model consisting of a systematic contribution $\boldsymbol{\varepsilon}_{\mathbf{es}}$ that is the same for all time-lapse steps, and a random observational error $\boldsymbol{\varepsilon}_{\mathbf{e},p}$ (p = 0, 1, 2, ... P, where P is the number of time steps) that is different for each time-lapse data set [e.g., *LaBrecque and Yang*, 2001] but assumed to stem from the same zero-mean Gaussian distribution. The observed data at time 0 are thus

$$\mathbf{d}_{\mathbf{e},0}^{obs} = g(\mathbf{m}_{\mathbf{e},0}) + \boldsymbol{\varepsilon}_{\mathbf{es}} + \boldsymbol{\varepsilon}_{\mathbf{e},0}, \tag{1}$$

with the forward response $g(\mathbf{m}_{\mathbf{e},0})$. The main contribution to the background residual

$$\mathbf{r}_{\mathbf{e},0} = \mathbf{d}_{\mathbf{e},0}^{obs} - g(\mathbf{m}_{\mathbf{e},0}) = \boldsymbol{\varepsilon}_{\mathbf{es}} + \boldsymbol{\varepsilon}_{\mathbf{e},0} \tag{2}$$

is the systematic error $\boldsymbol{\varepsilon}_{\mathbf{es}}$, which is a combination of modeling errors and systematic measurement errors due to ground coupling problems or geometrical errors. It is largely removed from the time-lapse data by using the differences $\tilde{\mathbf{d}}_{\mathbf{e},p}^{obs}$ (for time step p), to invert for the model update $\boldsymbol{\delta}\mathbf{m}_{\mathbf{e},p}$, where

$$\tilde{\mathbf{d}}_{\mathbf{e},p}^{obs} = \mathbf{d}_{\mathbf{e},p}^{obs} - \mathbf{r}_{\mathbf{e},0} = g(\mathbf{m}_{\mathbf{e},0} + \delta\mathbf{m}_{\mathbf{e},p}) + \boldsymbol{\varepsilon}_{\mathbf{e},p} - \boldsymbol{\varepsilon}_{\mathbf{e},0} . \quad (3)$$

This formulation improves ERT time-lapse inversion results, where typically $\boldsymbol{\varepsilon}_{\mathbf{es}} > \sqrt{\boldsymbol{\varepsilon}_{\mathbf{e},0}^2 + \boldsymbol{\varepsilon}_{\mathbf{e},p}^2}$ due to permanently installed electrodes and stable coupling conditions. In our case, we assume that $\boldsymbol{\varepsilon}_{\mathbf{es}}$ is 5 times larger than $\boldsymbol{\varepsilon}_{\mathbf{e},p}$.

For the first-arrival GPR data, we assume that the constant and systematic error contribution is smaller than the errors associated with picking, time-zero, and antennae positioning for each time-lapse data set. We thus solve for $\delta\mathbf{m}_{\mathbf{r},p}$ using (at time step p)

$$\mathbf{d}_{\mathbf{r},p}^{obs} = g(\mathbf{m}_{\mathbf{r},0} + \delta\mathbf{m}_{\mathbf{r},p}) + \boldsymbol{\varepsilon}_{\mathbf{r},p} . \quad (4)$$

Our inversions for $\delta\mathbf{m}_{\mathbf{e},p}$ and $\delta\mathbf{m}_{\mathbf{r},p}$ proceeds iteratively by decreasing the weight that penalize deviations from $\mathbf{m}_{\mathbf{e},0}$ and $\mathbf{m}_{\mathbf{r},0}$, as quantified by an exponential covariance function, until the residuals are as large as the assumed data errors [*Linde et al.* 2006]. Tests using models from the previous time step as background models gave inferior results, as artifacts appeared at previously occupied positions of the plume.

2.2. Joint inversion strategy

Coupling between the ERT and GPR time-lapse updates $\delta\mathbf{m}_{\mathbf{e},p}$ and $\delta\mathbf{m}_{\mathbf{r},p}$ is introduced in the inversion by cross-gradient constraints [*Gallardo and Meju*, 2004]. The cross-gradients function of the model updates at time-step p

$$\boldsymbol{\tau}_p(x,y,z) = \nabla\delta\mathbf{m}_{\mathbf{e},p}(x,y,z) \times \nabla\delta\mathbf{m}_{\mathbf{r},p}(x,y,z) \quad (5)$$

is discretized with a central-difference scheme and subsequently linearized. Deviations from zero of the discretized τ_p are heavily penalized at all discretized locations x, y, z of the inversion domain with a constant weight for all inversion steps. The joint inversion proceeds as for the individual inversions, but with the additional cross-gradient constraints.

The assumption of structural similarity between $\delta\mathbf{m}_{\mathbf{e},p}$ and $\delta\mathbf{m}_{\mathbf{r},p}$, as quantified by equation (5), is valid when only one state variable varies with time or when the methods employed are sensitive to the same physical property (e.g., electrical conductivity). The assumption holds for vadose zone tracers that have the same electrical conductivity as the pore water such that time-lapse ERT and GPR data only sense changes in moisture content. Simulations and joint inversions of field data acquired following saline tracer injection (not shown here) reveal that $\delta\mathbf{m}_{\mathbf{e},p}$ and $\delta\mathbf{m}_{\mathbf{r},p}$ are not structurally similar and that the resulting inversion models display artifacts.

3. Results

3.1. Site characteristics

At Hatfield in the UK, a test site was developed to study flow and transport in unsaturated media [for details see *Binley et al.*, 2002a]. The dominant sub-lithology at the site is medium grained sandstone, but with fine and medium sandstone sub-horizontally laminated on a millimeter scale (occurring in 0.2-0.5 m thick units, spaced at 1-3 m vertical intervals). *Binley et al.* [2002a] document a water tracer test carried out at the Hatfield site; here we use geophysical data from this test to illustrate our approach in a field setting. The center of mass and the spread of geophysically-defined plumes using individually inverted time-lapse data were previously used to characterize the hydrodynamics at Hatfield based on individual inversions and allowed deriving field-scale properties such as effective hydraulic conductivity [*Binley et al*., 2002a].

For the ERT measurements, 16 stainless steel electrodes were installed at 0.73 m intervals between a depth of 2 and 13 m in four boreholes in a trapezoid-like manner with side-lengths varying between 5 and 8 m. For the GPR measurements, two boreholes (along the *x*-axis) were drilled with 5 m spacing in-between one of the diagonals formed by the ERT boreholes.

Between 14:30 on 7 October and 13:40 on 10 October 1998, 2100 l of water tracer was injected at a uniform rate of approximately 30 l/h in a borehole slotted between 3 and 3.5 m depth located in-between the two GPR boreholes (x=3; y=4). To obtain a pure flow (no transport) experiment, the conductivity of the injected water was chosen to match the conductivity of the pore water. Multiple ERT and GPR data sets were acquired before and after tracer injection. We concentrate below on the time-lapse data set recorded directly after the end of injection (day 3) and two days later (day 5).

3.2. Synthetic example

A synthetic example mimicking the Hatfield water injection experiment was first used to evaluate our time-lapse joint inversion. We use a FEFLOW v6.0 Richards' equation solution assuming a uniform geological media. For this we discretized a region 8 m by 10 m (in plan) and 12 m deep into 73,202 6-node triangular-prism linear finite elements, with specific refinement around the tracer injection area. The lower boundary of the region defined a water table, and hence Dirichlet boundary conditions. The saturated hydraulic conductivity for all elements was set to 4.63×10^{-6} ms^{-1}, which is consistent with *Binley et al.* [2002a]. We used the widely adopted *van Genuchten* [1980] representation of unsaturated hydraulic characteristics, with a residual saturation of 0.0025, exponent $n_{vG} = 1.964$ and $\alpha_{vG} = 4.1$ m^{-1}. In order to develop more natural initial conditions we first setup a uniform saturation of 0.5 within the model and then ran a 20 day drainage period. The tracer was then imposed within the model and the tracer movement was simulated with a maximum time step of 0.05 days. Synthetic GPR and ERT data were simulated using interpolated moisture content θ at days 0, 3 and 5. The bulk electrical resistivity ρ was calculated as a function of saturation $S = \theta/\phi$ (where ϕ is porosity) using Archie's second law [*Archie*, 1942]

$$\rho = \rho_s S^{-n}, \tag{6}$$

where $\rho_s = 66\ \Omega$m is the bulk resistivity at full saturation and $n = 1.13$ is Archie's saturation exponent determined from three samples of the main lithology at the Hatfield site [see *Binley et al*., 2002b].

The relative permittivity κ was calculated using the complex refractive index model (CRIM) [*Birchak et al*., 1974]

$$\sqrt{\kappa} = (1-\phi)\sqrt{\kappa_s} + \theta\sqrt{\kappa_w} + (\phi-\theta)\sqrt{\kappa_a} \tag{7}$$

where $\kappa_w = 81$ and $\kappa_a = 1$ are the relative permittivities of water and air, respectively. The porosity $\phi = 0.32$ and the relative permittivity of the sediment grains $\kappa_s = 5$ were obtained from lab measurements on retrieved cores [*West et al*., 2003]. Radar slowness, *s*, was calculated from the permittivity using $s = \sqrt{\kappa}/c$, with *c* the speed of light in a vacuum.

Forward solvers were used to calculate electrical resistances and radar traveltimes for these models. The electrical responses and related sensitivities were computed using a finite-element solver implemented by *Rücker et al*. [2006], and the traveltimes and sensitivities were calculated in the high frequency limit using a finite-difference algorithm [*Podvin and Lecomte*, 1991]. The ERT measurement scheme included a variety of four-electrode configurations using electrodes in a varying number of boreholes and the data were filtered to only include configurations with a geometrical factor of less than 600. The multiple-offset gathers were calculated using 0.25 m intervals between antenna positions over the range 0-11 m below ground level for cases when the angle between the transmitter and receiver antennas were within ±45° from the horizontal. For each time-step, the resulting data sets of 833 resistances and 1181 multiple offset GPR traveltimes were contaminated by Gaussian noise according to the error models of equations (1)-(4) with zero mean and standard deviations $std(\boldsymbol{\varepsilon}_{es}) = 2.5\%$, $std(\boldsymbol{\varepsilon}_{e,0}) = std(\boldsymbol{\varepsilon}_{e,p}) = 0.5\%$ and

$std(\boldsymbol{\varepsilon}_{\mathbf{r},0}) = std(\boldsymbol{\varepsilon}_{\mathbf{r},p})$ = 0.5% + 0.5 ns. The same configurations and data error descriptions were also used to invert the field data described below.

The background data sets (i.e., before water injection) were inverted individually in 3-D (not shown) and the time-lapse data were inverted both individually and jointly in 3-D using a regular inversion grid with voxel side lengths of 0.35 m. Integral scales of the exponential covariance model used to regularize the inversion of the background data set was 2 m in the horizontal and 1 m in the vertical direction to respect the independently observed anisotropy at the field site. The integral scale chosen for the time-lapse inversion was 0.7 m in all directions, corresponding to the expected length scale at which the tracer plume might be resolved. Values in the range of 0.5-1.0 m provide similar results. After 10 iterations, all inversion models fit the data to the specified error level with the largest possible weight to the model regularization.

The water content was calculated from the resulting models using equations (6) and (7) with the petrophysical parameters mentioned above. Vertical profiles of the inferred time-lapse change in moisture content, $\Delta\theta$, from the background model are shown in Figure 1. It is seen that the magnitude of $\Delta\theta$ is rather well estimated in the GPR inversion but markedly underestimated in the ERT inversion for both the individual and joint inversions, which can be explained by the more significant resolution limitations of ERT inversions [*Day-Lewis et al*., 2005].

To quantify the changes we define a plume boundary, for each model, at 1/3 of the maximum $\Delta\theta$. These plumes were then used to calculate the mass, center of mass and the variances of the plumes, with the resulting statistics presented in Table 1. This plume definition is rather simplistic [c.f., *Day-Lewis et al.*, 2007], but the relative differences between the individual and joint inversions are similar for other cut-off values, and serves here only to investigate if the plume definition is improved by the joint inversion. Note that the 3-D shape of

the plume is heavily dependent on the regularization used as the data sets are acquired between pairs of boreholes.

The individual GPR inversion model overestimates the mass (+46% (+58%) for day 3 (day 5)), whereas it is more reasonable for the joint inversions (+5% (+13%) for day 3 (day 5)). These results indicate that the ERT data helps to constrain the geometry of the GPR model that otherwise is only based on data acquired along one plane and extended in 3-D based on the regularization. The individual (-49% (-56%) for day 3 (day 5)) and joint ERT (-61% (-51%) for day 3 (day 5)) models significantly underestimate the mass with no improvement for the joint inversions.

The error in the center of mass from the individual GPR (0.47 m (0.20 m) for day 3 (day 5)) and ERT inversions (0.42 m (0.34 m) for day 3 (day 5)) are improved in the joint inversion (0.18 m and 0.17 m, respectively) for day 3, but less so for day 5 (0.20 m and 0.25 m, respectively). The horizontal variances of the estimated GPR and ERT plumes from the joint inversions are less overestimated (+100 % on average) than for the individual inversions (+190 % on average). This is due to resolution improvements of joint inversions of crosshole data that are the most important in the horizontal direction [*Linde et al*., 2008].

3.3. Hatfield 1998 water injection

Our time-lapse inversion methodology was then applied to the Hatfield field data. Radar transmission data were acquired using Sensors and Software's Pulse EKKO radar system with 100 MHz antennas. ERT measurements were acquired using the DMT Resecs resistivity instrument. The background data sets were inverted individually in 3-D and the final models (not shown) are consistent with the known geology and fit the data to the specified error levels (see

previous section). The time-lapse data were inverted both individually and jointly in 3-D for 12 iterations such that all inversion results fit the prescribed error level.

Figure 2 shows vertical profiles of the inferred $\Delta\theta$ using equations (6) and (7) with the specified parameter values. These results are consistent with the synthetic example in that the joint inversion models are more focused. Scatter plots of the inversion results show that the scatter observed in the individual inversions (Figures 3a and 3c) is much reduced and that the $\Delta\theta$ magnitudes are increased in the joint inversions (Figures 3b and 3d). The plumes defined by the fractional thresholding procedure were then used to calculate the center of mass and the variances of the plumes (see Table 2). The individual GPR inversion model overestimates the injected mass of 2100 *l* (+39% (+57%) for day 3 (day 5)), whereas it is more reasonable for the joint inversions (+4% (+37%) for day 3 (day 5)). The individual (-50% (-53%) for day 3 (day 5)) and joint ERT (-56% (-54%) for day 3 (day 5)) models both underestimate the mass with no improvement for the joint inversions.

The differences in the center of mass between the individual GPR and ERT models (0.35 m (0.34 m) for day 3 (day 5)) are improved for the joint inversion at both time-steps (0.05 m (0.18 m) for day 3 (day 5)). The variance estimates of the GPR and ERT plumes are smaller in the horizontal direction for the joint compared to the individual inversions (24% on average) indicating that the joint inversion improves resolution.

4. Concluding remarks

A synthetic experiment based on flow simulations together with field data from a water injection experiment in unsaturated sandstone show clearly that cross-gradients joint inversion of crosshole time-lapse ERT and GPR traveltime data decrease horizontal smearing of plumes, that they increase the similarity between models, and the estimated center of mass of plumes

compared to individual time-lapse inversions. The examples also illustrate that higher resolution 2-D traveltime GPR data might benefit from lower resolution 3-D ERT data. We emphasize that the inversion methodology presented here is only valid when one state variable varies at each location of the model domain. For example, if the fluid salinity of the tracer was different to the native pore water salinity then the resistivity would be a function of moisture content and salinity, which would violate the assumptions of structural similarity underlying the cross-gradient constraints.

Acknowledgements

The field data were acquired by P. Winship and R. Middleton, formerly of Lancaster University. We thank T. Günther, A. Tryggvason and collaborators for providing the ERT and traveltime forward solvers. A. Binley is grateful to A. Green at ETHZ for generous support that enabled his contribution. We thank Frederick Day-Lewis and Luis Gallardo for their reviews. Funding was provided by the Swiss National Science Foundation.

References

Archie, G. E. (1942), The electrical resistivity log as an aid in determining some reservoir characteristics, *Tech. Rep. 1422*, Am. Inst. Min. Metall. Pet. Eng., New York.

Binley, A., G. Cassiani, R. Middleton, and P. Winship (2002a), Vadose zone flow model parameterisation using cross-borehole radar and resistivity imaging, *J. Hydrol.*, *267*, 147-159, doi:10.1016/S0022-1694(02)00146-4.

Binley, A., P. Winship, L. J. West, M. Pokar, and R. Middleton (2002b), Seasonal variation of moisture content in unsaturated sandstone inferred from borehole radar and resistivity profiles, *J. Hydrol*., *267*, 160-172, doi:10.1016/S0022-1694(02)00147-6.

Birchak, J. R., C. G., Gardner, J. E. Hipp, and J. M. Victor (1974), High dielectric constant microwave probes for sensing soil moisture, *Proceedings of the IEEE*, *62*, 93-98.

Day-Lewis, F. D., K. Singha, and A. M. Binley (2005), Applying petrophysical models to radar travel time and electrical resistivity tomograms: Resolution dependent limitations, *J. Geophys. Res*., *110*, B08206, doi:10.1029/2004JB003569.

Day Lewis, F. D., Y. Chen, and K. Singha (2007), Moment inference from tomograms, *Geopys. Res. Lett*., *34*, L22404, doi:10.1029/2007GL031621.

Gallardo, L. A., and M. A. Meju (2004), Joint two-dimensional DC resistivity and seismic travel time inversion with cross-gradients constraints, *J. Geophys. Res.*, *109*(B3), B03311, doi:10.1029/2003JB002716.

LaBrecque, D. J., and X. Yang (2001), Difference inversion of ERT data: a fast inversion method for 3-D in situ monitoring, *JEEG*, *6*(2), 83-89, doi:10.4133/JEEG6.2.83.

Linde, N., A. Binley, A. Tryggvason, L. B. Pedersen, and A. Revil (2006), Improved hydrogeophysical characterization using joint inversion of cross-hole electrical resistance and ground-penetrating radar traveltime data, *Water Resour. Res.*, *42*(12), W12404, doi:10.1029/2006WR005131.

Linde, N., A. Tryggvason, J. Peterson, and S. Hubbard (2008), Joint inversion of crosshole radar and seismic traveltimes, *Geophysics,* 73*,* G29-G37, doi:10.1190/1.2937467.

Podvin, P., and I. Lecomte (1991), Finite difference computation of traveltimes in very contrasted velocity models: a massively parallel approach and its associated tools, *Geophys. J. Int*., 105, 271-284, doi:10.1111/j.1365-246X.1991.tb03461.x.

Rücker, C., T. Günther, and K. Spitzer (2006), Three-dimensional modelling and inversion of dc resistivity data incorporating topography - I. Modelling, *Geophys. J. Int*., 166, 495-505, doi:10.1111/j.1365-246X.2006.03010.x.

Singha, K., and S. M. Gorelick (2005), Saline tracer visualized with three-dimensional electrical resistivity tomography: Field-scale spatial moment analysis, *Water Resources Research*, *41*, W05023, doi:10.1029/2004WR003460.

van Genuchten, M.Th. (1980), A closed-form equation for predicting the hydraulic conductivity of unsaturated soils, *Soil Sci. Soc. Am. J., 44*, 892–898.

West, L. J., K. Handley, Y. Huang, and M. Pokar (2003), Radar frequency dielectric dispersion in sandstone: Implications for determination of moisture and clay content, *Water Resour. Res.*, *39*(2), 1026, doi:10.1029/2001WR000923.

Figure and Table captions:

Figure 1. Vertical profiles of moisture content change ($\Delta\theta$) since the beginning of a synthetic water injection test as inferred from individual and joint inversion of time-lapse crosshole ERT and GPR traveltime data. (a) Through the injection point at the end of injection (day 3), (b) 3.5 m away from the injection point and the GPR acquisition plane at the end of injection (day 3), (c-d) same as (a-b) but two days after the end of injection (day 5).

Figure 2. As in Figure 1, but with data from the Hatfield 1998 water injection test.

Figure 3. Scatter plots of moisture content change ($\Delta\theta$) inferred from (a) individual and (b) joint time-lapse inversions of the Hatfield data at day 3, (c-d) same as (a-b) but for day 5. The black triangles indicate model cells with GPR ray coverage.

Table 1. Statistics of the geophysically-defined plumes for the synthetic example using cut-offs of 1/3 of the maximum moisture content change ($\Delta\theta$) for each geophysically-derived model. The ERT data and model weight in the joint inversions is 2.8 times that of the GPR to assure that both models converge to the same target data misfit.

Synthetic		Mass [m^3]	Center of Mass [m]			Variance [m^2]		
			x	y	z	σ^2_{xx}	σ^2_{yy}	σ^2_{zz}
Day 3	True	2.12	3.00	4.00	5.05	0.37	0.37	1.00
	GPR individual	3.06	2.54	3.89	5.07	1.36	1.05	0.61
	ERT individual	1.08	3.19	4.36	5.17	1.17	1.12	0.92
	GPR joint	2.20	2.92	4.16	5.07	0.90	0.76	0.57
	ERT joint	0.81	2.92	4.15	5.08	0.89	0.75	0.57
Day 5	True	2.08	3.00	4.00	6.01	0.55	0.55	1.43
	GPR individual	3.32	2.85	3.98	6.14	1.82	1.32	1.10
	ERT individual	0.93	3.05	4.34	6.04	1.36	1.34	0.98
	GPR joint	2.39	3.13	4.20	6.14	1.14	0.92	1.04
	ERT joint	1.02	3.10	4.20	6.12	1.06	0.83	0.99

Table 2. Statistics of the geophysically-defined plumes for the Hatfield water injection experiment. The ERT data and model weight is 1.8 times that of the GPR in the joint inversions to assure that both models converge to the same target data misfit.

Hatfield		Mass [m^3]	Center of Mass [m]			Variance [m^2]		
			x	y	z	σ^2_{xx}	σ^2_{yy}	σ^2_{zz}
Day 3	GPR individual	2.92	2.87	4.05	4.77	1.78	1.21	0.85
	ERT individual	1.06	3.07	4.24	4.99	0.79	0.96	0.86
	GPR joint	2.18	3.13	4.21	4.84	1.02	0.92	0.81
	ERT joint	0.93	3.10	4.17	4.85	0.87	0.76	0.70
Day 5	GPR individual	3.30	3.49	4.08	5.55	2.35	1.44	1.85
	ERT individual	0.85	3.28	4.34	5.47	1.42	1.29	1.19
	GPR joint	2.80	3.47	4.31	5.57	1.63	1.36	1.69
	ERT joint	0.92	3.34	4.23	5.66	1.11	0.84	1.19

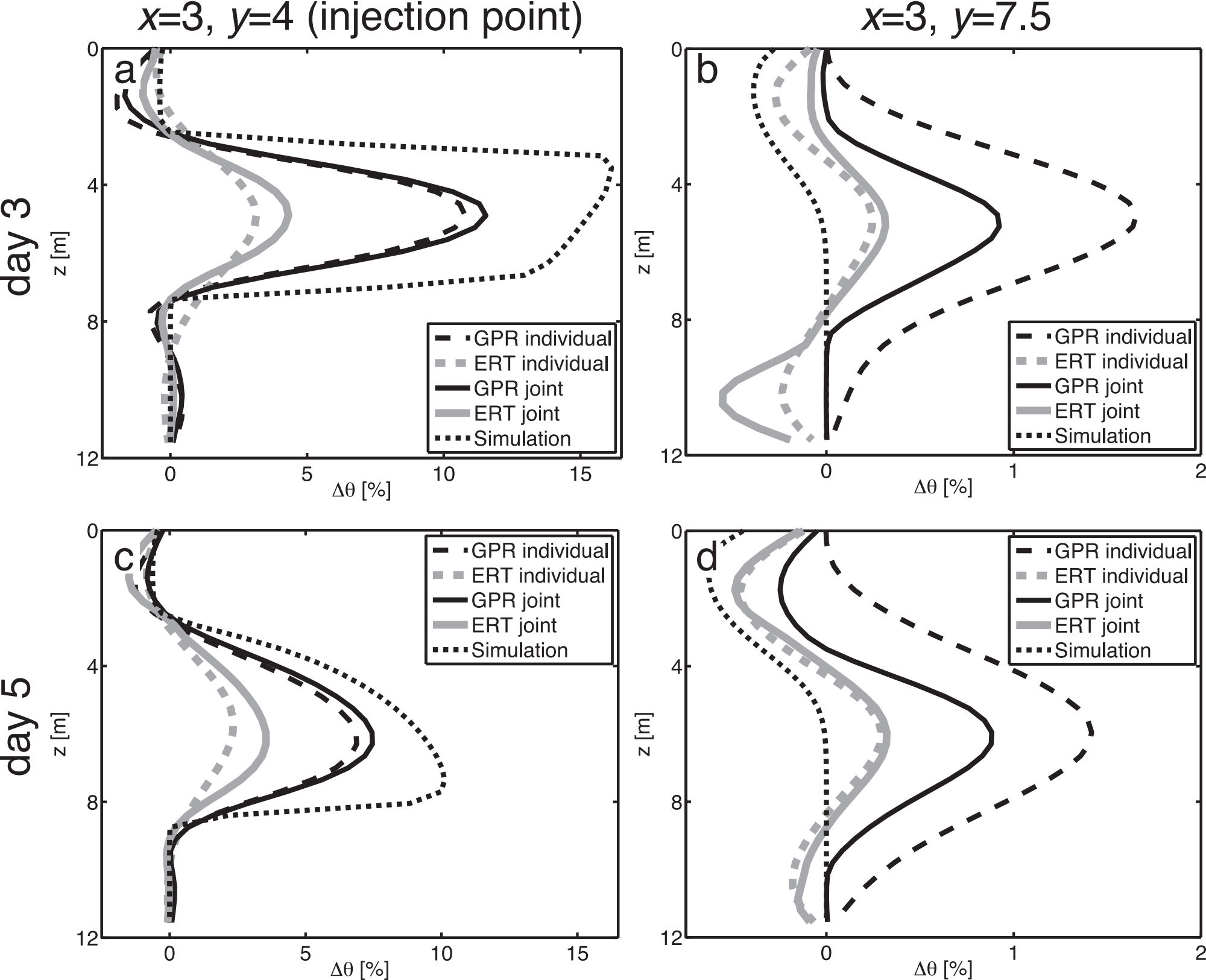
x=3, y=4 (injection point)
x=3, y=7.5
day 3
day 5
a
b
c
d
z [m]
Δθ [%]
GPR individual
ERT individual
GPR joint
ERT joint
Simulation
0
4
8
12
0
5
10
15
1
2

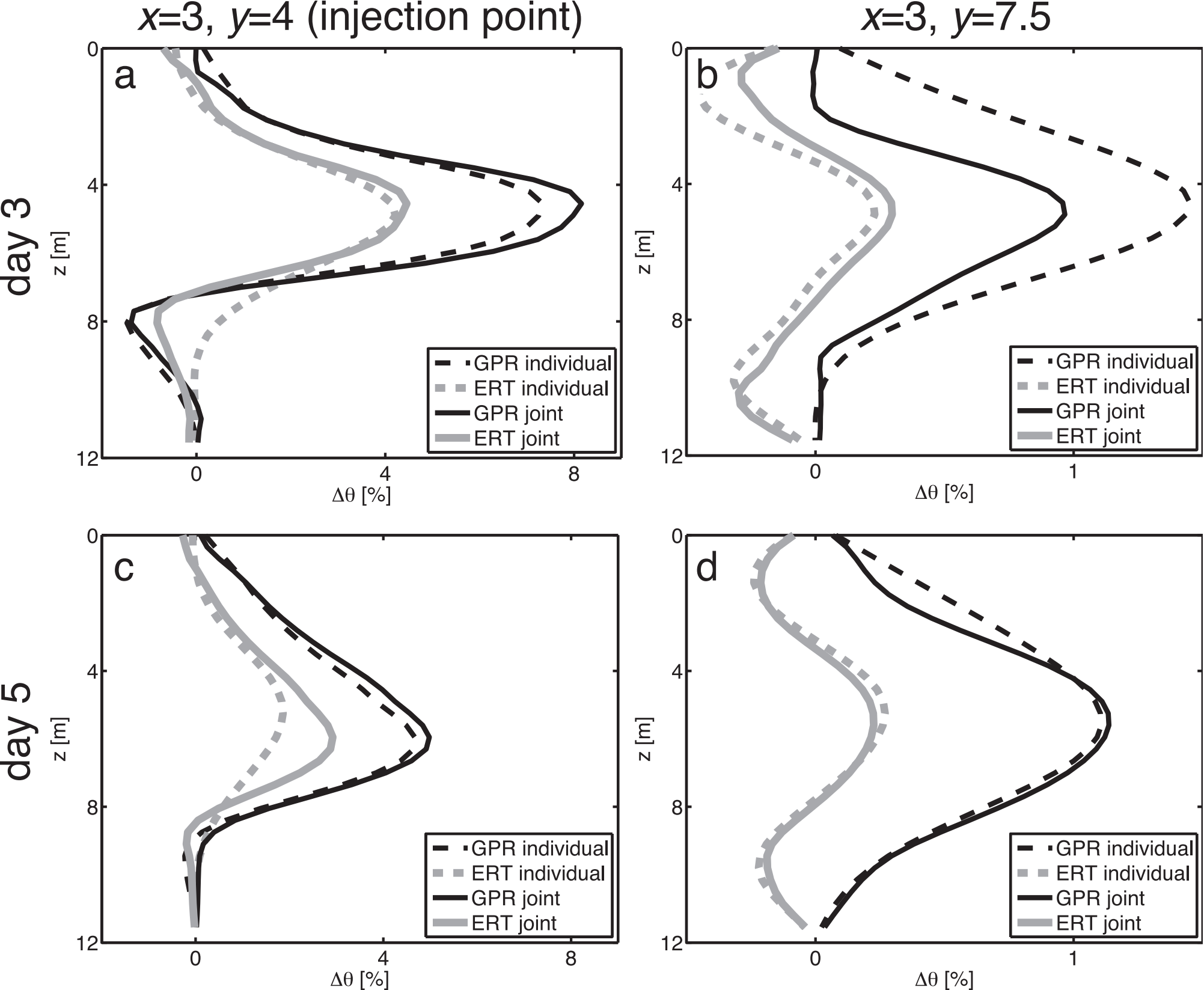
x=3, y=4 (injection point)
x=3, y=7.5
day 3
day 5
a
b
c
d
z [m]
Δθ [%]
0
4
8
12
1
GPR individual
ERT individual
GPR joint
ERT joint

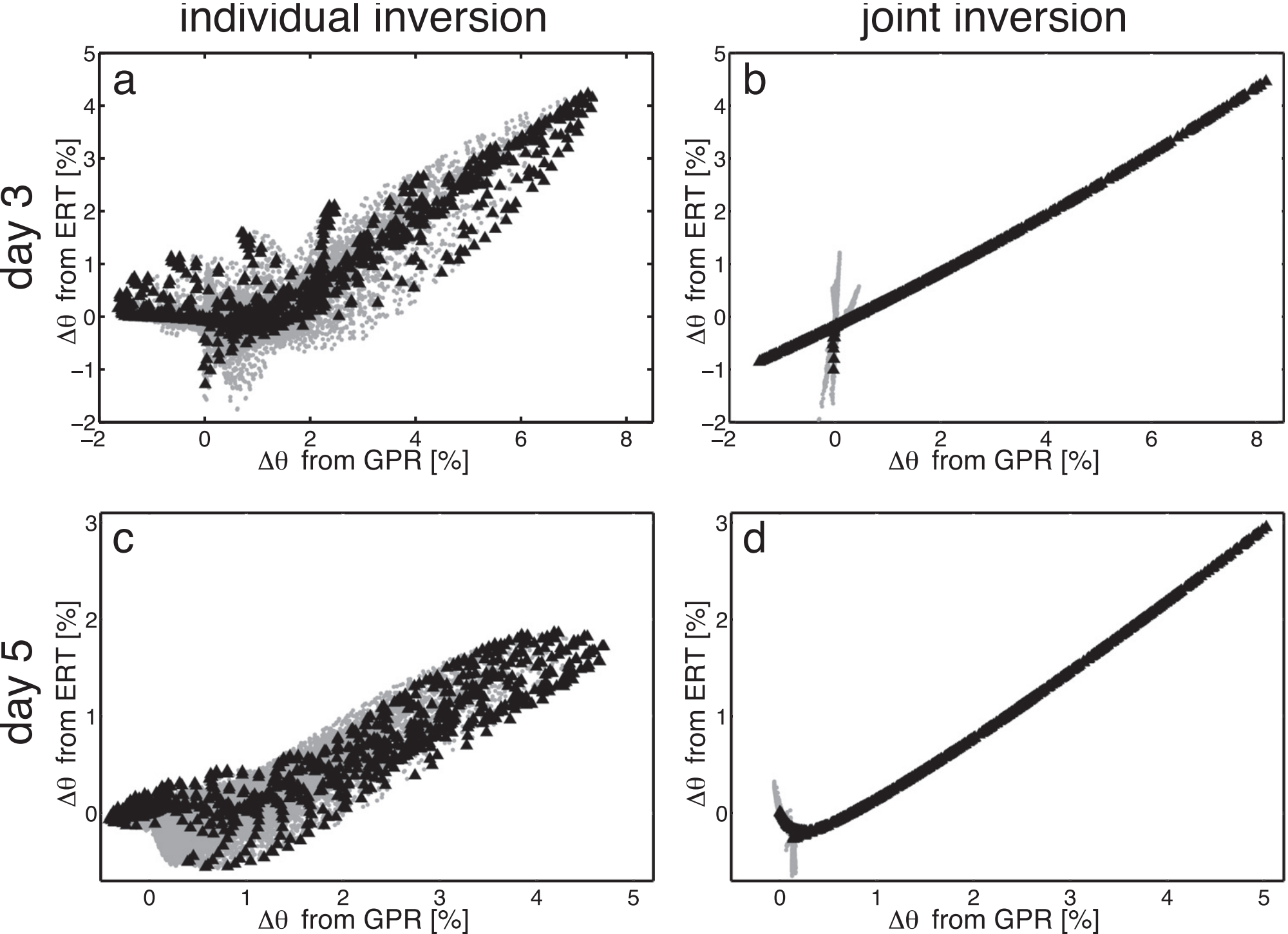
individual inversion
joint inversion
day 3
day 5
a
b
c
d
Δθ from ERT [%]
Δθ from GPR [%]